ROYAL SOCIETY
OF CHEMISTRY

PAPER

Check for updates

In situ growth of WO₃/BiVO₄ nanoflowers onto cellulose fibers to construct photoelectrochemical/colorimetric lab-on-paper devices for the ultrasensitive detection of AFP†

Xu Li,[a] Kang Cui, [iD] *[a] Mingzhen Xiu, [iD] [b] Chenxi Zhou,[a] Li Li,[a] Jing Zhang,[a] Shiji Hao,[c] Lina Zhang,[d] Shenguang Ge, [iD] [a] Yizhong Huang [iD] *[b] and Jinghua Yu [iD] *[a]

In this work, novel dual-mode lab-on-paper devices based on *in situ* grown WO₃/BiVO₄ heterojunctions onto cellulose fibers, as signal amplification probes, were successfully fabricated by the integration of photoelectrochemical (PEC)/colorimetric analysis technologies into a paper sensing platform for the ultrasensitive detection of alpha-fetoprotein (AFP). Specifically, to achieve an impressive PEC performance of the lab-on-paper device, the WO₃/BiVO₄ heterojunction was *in situ* grown onto the surface of cellulose fibers assisted with Au nanoparticle (Au NP) functionalization for enhancing the conductivity of the working zone of the device. With the target concentration increased, more immune conjugates could be captured by the proposed paper photoelectrode, which could lead to a quantitative decrease in the photocurrent intensity, eventually realizing the accurate PEC signal readout. To meet the requirement of end-user application, a colorimetric signal readout system was designed for the lab-on-paper device based on the color reaction of 3,3′5,5′-tetramethylbenzidine (TMB) oxidized by WO₃/BiVO₄ nanoflowers in the presence of H_2O_2. Noticeably, it is the first time that the WO₃/BiVO₄ heterojunction is *in situ* grown onto cellulose fibers, which enhances the sensitivity in view of both their PEC activity and catalytic ability. By controlling the conversion process of hydrophobicity and hydrophilicity on the lab-on-paper device combined with diverse origami methods, the dual-mode PEC/colorimetric signal output for the ultrasensitive AFP detection was realized. Under optimal conditions, the proposed dual-mode lab-on-paper device could enable the sensitive PEC/colorimetric diagnosis of AFP in the linear range of 0.09–100 ng mL^{-1} and 5–100 ng mL^{-1} with the limit of detection of 0.03 and 1.47 ng mL^{-1}, respectively.

Introduction

Alpha-fetoprotein (AFP), as one of the major components of proteins in human embryonic serum, is mainly generated from the yolk sac, germ cell, and liver organ.[1,2] Generally, the concentrations of AFP in the serum of the newborn and healthy adults are about 10–50 μg mL^{-1} and 25 ng mL^{-1},

respectively.[3–5] Although the concentration of AFP is low in serum, its concentration variation in serum has been identified to be associated with several diseases such as yolk sac tumor, hepatocellular carcinoma (HCC), and certain gastric carcinomas.[6–12] Therefore, it is well worth to exploit effective strategies with advantageous techniques for the ultrasensitive determination of AFP.

Till date, several approaches based on various techniques for detecting AFP have been reported, including electrochemical,[13,14] electrochemiluminescence (ECL),[15] fluorescence,[16] and enzyme-linked immunosorbent assay (ELISA).[17] However, these strategies could not avoid potential challenges such as time consumption, high detection cost, and unsuitability for rapid analysis. To address these concerns, the photoelectrochemical (PEC) technique that integrates photochemistry with electrochemistry has been extensively explored for bioassays in recent years[18,19] due to its inherent merits such
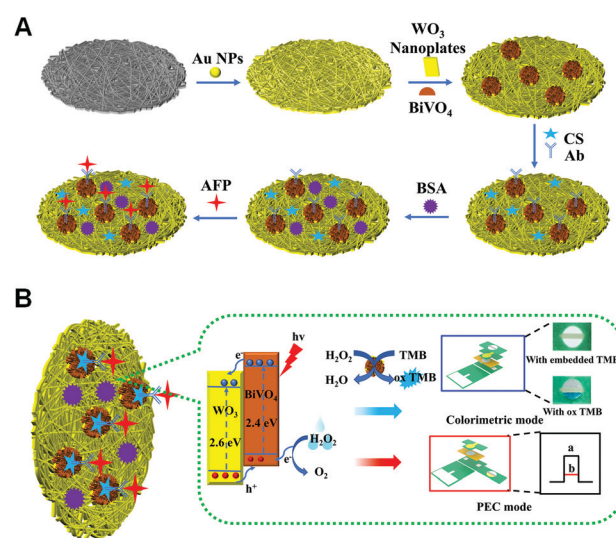
[a] *School of Chemistry and Chemical Engineering, University of Jinan, Jinan 250022, P. R. China. E-mail: chm_cuik@ujn.edu.cn, ujn.yujh@gmail.com*

[b] *School of Materials Science and Engineering, Nanyang Technological University, Singapore 639798, Singapore. E-mail: yzhuang@ntu.edu.sg*

[c] *School of Materials Science & Engineering, Dongguan University of Technology, Guangdong 523808, P. R. China*

[d] *Shandong Provincial Key Laboratory of Preparation and Measurement of Building Materials, University of Jinan, Jinan, 250022, P. R. China*

† Electronic supplementary information (ESI) available. See DOI: https://doi.org/10.1039/d2tb00297c

as high sensitivity, easy operation with simple instrumentation, and low background signal.[20,21] Unlike the conventional electrochemical sensing system for which normally a specific bias has to be applied for producing readout signals, the PEC sensing system can sufficiently reduce the dependence on potential application for signal generation resulting from the enhanced redox property of photoelectric materials with efficient carrier separation ability. Besides, the PEC sensing system possess two separate source parts for signal excitation and detection, making it a potentially higher sensitivity sensing technique because of the reduced background noise.[22–27] In the PEC sensing process, electron-hole pair separation and charge transfer occur on the photoactive material under light irradiation, resulting in photoelectric signal conversion, and further inducing a great change in the corresponding light response, which is normally decided by the properties of photoactive materials.[20,22] Therefore, to achieve a highly sensitive PEC platform for detecting AFP, it is extremely important to explore photoactive materials that play a key role for its construction.[28] Semiconductor materials are widely applied to construct novel photoactive materials due to their satisfied electronic states of the valence band and conduction band as well as suitable bandgaps.[21] In particular, oxide semiconductor materials, as a typical semiconductor, have been explored for the development of photoactive materials over the past few years, such as TiO_2,[29–31] WO_3,[32,33] ZnO,[34–37] and SnO_2.[38] Of these, WO_3, as a low-cost metal oxide semiconductor, is an indirect bandgap photoactive material with favorable photoconductive behaviors, which can absorb a wide range of wavelengths including part of visible light based on its moderate bandgap (2.5–2.7 eV), and good electron transport properties on account of its appropriate band-edge position.[39] For all that, however, WO_3 alone as a photoanode material still overcomes the limitations such as poor charge separation, fast recombination of photo-generated electron-hole pairs, long hole diffusion length, and less utilization of solar irradiation due to the narrow photoresponse region (≤ 460 nm) in PEC applications.[40,41] To address this problem, forming binary nanocomposites *via* hybridizing WO_3 with proper bandgap semiconductors is one of the effective strategies to improve the PEC performance of WO_3.[42] $BiVO_4$, as a typical semiconductor with a moderate band gap ($\sim$2.4 eV), high stability against photocorrosion, and a high specific surface area of various well-defined morphologies, has been proven to be one of the most potential sensitizers for adjusting the bandgap of semiconductors, and applied for biomedical developments with its toxic free nature, low cost, and long-term chemical stability.[43–47] In such case, WO_3/$BiVO_4$ nanocomposites could not only integrate the merits of WO_3 with good electron transport rate and $BiVO_4$ with broad light absorption range, but also effectively realize the separation of photogenerated carriers for further enhancing the photocurrent response.[42] Besides, WO_3/$BiVO_4$ nanocomposites could catalyze 3,3′5,5′-tetramethylbenzidine (TMB) to be oxidized with H_2O_2 due to its peroxidase mimic activity, and achieve colorimetric detection applications.[48]

In recent years, the cellulose paper has attracted extensive attention due to its inherited merits of good biocompatibility, easy functionalization, and acceptable biodegradability in the

fabrication of portable diagnostic devices.[49–57] Thus far, some lab-on-paper devices such as paper-based colorimetric biosensors,[58] paper-based electrochemical analytical devices,[59,60] enzyme-based paper biosensors,[61] and self-powered origami paper analytical devices based on various techniques have been developed.[62] What is more, since the cellulose paper has a unique porous structure, rough surface properties, and a large surface-to-volume ratio, the majority nanomaterials and functional groups could be modified on the surface of cellulose fibers, meeting the requirement as a satisfied substrate to construct biosensing platforms.

Herein, we propose a dual-mode PEC/colorimetric lab-on-paper device based on the *in situ* growth of WO_3/$BiVO_4$ heterojunctions onto cellulose fibers for highly sensitive AFP detection on account of their enhanced PEC activity and catalytic ability. At first, to realize the PEC mode, the WO_3/$BiVO_4$ heterojunction was *in situ* grown onto the surface of cellulose fibers, where a layer of Au NPs was grown for improving the electron transport rate, by a hydrothermal method, as illustrated in Scheme 1A. Then, the AFP antibodies (Ab) were immobilized onto a WO_3/$BiVO_4$ heterojunction-functionalized Au NP-modified paper working electrode (Au-PWE) using chitosan (CS) and glutaraldehyde (GLD) to capture AFP targets. By introducing bovine serum albumin (BSA) to avoid any nonspecific interaction, the AFP can be specifically recognized and connected *via* specific recognition on the photoanode surface of the proposed device, eventually achieving the ultrasensitive detection of AFP as the photocurrent response decreased based on the effective H_2O_2 electron donor consumption and apparent steric hindrance. To reach the colorimetric detection of AFP, WO_3/$BiVO_4$ nanoflowers were involved in the chromogenic region by a delicate design of the lab-on-paper device and

Scheme 1 (A) Fabrication procedure of the lab-on-paper PEC sensing platform. (B) Schematic illustration of the PEC/colorimetric analytical principle. (Colorimetric mode: the folding state of the lab-on-paper device shown in blue rectangle and the colorimetric results before and after incubation of AFP; PEC mode: the folding state of the lab-on-paper device shown in red rectangle and the PEC signal before and after incubation of AFP.)

4032 | *J. Mater. Chem. B*, 2022, **10**, 4031–4039

This journal is © The Royal Society of Chemistry 2022

utilized to efficiently catalyze the oxidation of embedded TMB in the presence of H_2O_2, successfully realizing the semi-quantitative AFP target detection using a colorimetric signal readout. As a result, the dual-mode PEC/colorimetric lab-on-paper device based on the *in situ* growth of $WO_3/BiVO_4$ hetero-junctions onto cellulose fibers for ultrasensitive AFP detection was finally constructed. Besides, the good feasibility of the as-prepared lab-on-paper device applied in real blood serum sample detection was investigated, indicating the great potential applications in the point-of-care testing of AFP and clinical disease diagnosis.

Experimental section

Materials and reagents

All aqueous solutions were prepared with deionized water (DI water, resistivity ≥ 18.25 MΩ cm^{-1}), which was obtained from a Millipore water purification system. KCl, NaWO$_3$ and NH$_4$VO$_3$ were purchased from Maclean Biochemical Technology Co., Ltd (Shanghai, China). Sodium hydroxide (NaOH) and Bi(NO$_3$)$_3$·5H$_2$O, were provided by Aladdin (Shanghai, China). KH$_2$PO$_4$, Na$_2$HPO$_4$, (NH$_4$)$_2$C$_2$O$_4$ and urea were obtained from Tianjin Damao Chemical Reagent Company (Tianjin, China). Chlor-oauric acid (HAuCl$_4$·4H$_2$O) and hydrogen peroxide (H$_2$O$_2$) were ordered from Sangon Biological Engineering Technology and Services Co., Ltd (Shanghai, China). 3,3′,5,5′-Tetramethyl-benzidine (TMB) and acetic acid were purchased from Shanghai Jizhi Biochemical Technology Co., Ltd (Shanghai, China). Bovine serum albumin (BSA) was obtained from Sigma-Aldrich Chemical Co. Phosphate-buffered saline (PBS, pH 7.4, 0.1 M) was prepared with Na$_2$HPO$_4$ (0.1 M), KH$_2$PO$_4$ (0.1 M), and KCl (0.1 M). Chitosan (CS) was purchased from Solarbio Co., Ltd (China). Glutaraldehyde (GLD; 50%) was purchased from Tianjin Chemical Plant Co., Ltd (Tianjin, China). Alpha-fetoprotein (AFP), fetoprotein antibody (anti-AFP), carcino-embryonic antigen (CEA) and prostate-specific antigen (PSA) were purchased from Shanghai Linc-Bio Science Co., Ltd (Shanghai, China). Human immunoglobulin G (H-IgG) was obtained from Shanghai Sangon Biotech Co., Ltd (China). All chemicals were used without further purification. Whatman chromatography paper #2 (58.0 cm × 68.0 cm) was received from GE Healthcare Worldwide (Shanghai, China), and it was cut into A4 size before use.

Apparatus and measurements

The photocurrent response and electrochemical impedance spectroscopy (EIS) were performed using a CHI 660D electro-chemical workstation (Shanghai CH Instruments Co., China) with a strand three-electrode system consisting of the working, reference, and counter electrodes. Ultraviolet-visible (UV-vis) absorption spectra were recorded using a UV-2550 spectro-photometer (Shimadzu, Kyoto, Japan). Scanning electron microscopic (SEM) analyses were performed using a QUANTA FEG 250 thermal field emission SEM (FEI Co., USA) equipped with an Oxford X-MAX50 X-ray energy-dispersive spectrometer

(EDS) (Oxford Co., UK). Transmission electron microscopic (TEM) images were acquired using a JEOL 4000 EX microscope. Infrared spectra were recorded using a Fourier transform infrared (FT-IR) Spectrum RX (PerkinElmer Spectoment). X-ray photoelectron spectroscopy (XPS) spectra were recorded using an ESCALAB MK II X-ray photoelectron spectrometer. X-ray diffraction (XRD) patterns were acquired using a Pa D8 advance diffractometer system equipped with a Cu Kα radiation source (Bruker Co., Germany). Raman spectrum was recorded using a Labram HR evolution spectrometer (Horiba jobin yvon Corporation, French). The EIS experiments were carried out in PBS (pH 7.4, 0.1 M) containing 5.0 mM [Fe(CN)$_6$]$^{3-/4-}$ with 0.1 M KCl. Photocurrent response measurements were done in PBS (pH 6.5, 0.1 M) at room temperature with 200 μL of H$_2$O$_2$ (5 mM). During the PEC measurement procedure, a Xe lamp was used as the excitation light source, and the applied potential was 0.4 V.

Preparation of WO$_3$ nanoflakes on the paper-based electrode

The preparation of a WO$_3$ lab-on-paper device was similar to a previous protocol.[33] Before the WO$_3$ nanoflakes were modified to the paper electrode, a layer of Au nanoparticles was dropped to the paper work zone. Due to the high conductivity of Au nanoparticles, the WO$_3$ nanoflakes are easy to grow on the work zone *in situ*. First, 0.5 g sodium tungsten (Na$_2$WO$_3$) was dissolved in 30 mL of deionized water under stirring at room temperature, and then 10 mL of 2.0 M HCl was slowly added into this solution. Subsequently, 0.4562 g of ammonium oxa-late ((NH$_4$)$_2$C$_2$O$_4$) was added into 30 mL of deionized water under stirring. By mixing this solution under stirring for 30 minutes, a clear and transparent solution was obtained. The prepared precursor was transferred into a 100 mL Teflon-lined stainless autoclave. The lab-on-paper device was immersed and leaned against the wall of the Teflon vessel with the conducting side face down. After that, the Teflon-lined stainless autoclave was put into an oven at 160 °C for 1 h. Finally, the lab-on-paper device with WO$_3$ nanoflakes was washed with deionized water and dried at 60 °C overnight.

Preparation of WO$_3$/BiVO$_4$ paper-based photoelectrodes

The synthesis method of BiVO$_4$ is based on a procedure previously reported in the literature with minor modifica-tions.[63] Briefly, 4.3 mM NH$_4$VO$_3$ and 5.2 mM Bi(NO$_3$)$_3$·5H$_2$O were dissolved in 40 mL deionized water under stirring and named solution A. Then, 20 mL deionized water was dissolved in 25 mM urea and named solution B. Solution B was dropped into solution A at a rate of 60 drops per minute after urea was completely dissolved. When a homogeneous orange solution was obtained, it was moved into a 100 mL Teflon-lined stainless autoclave with the conductive side of the WO$_3$ nanoflake electrode facing down. After that, the Teflon-lined stainless autoclave was kept in an oven at 180 °C for 4 h. Finally, the WO$_3$/BiVO$_4$ paper-based electrode was washed thoroughly with deionized water and dried at 60 °C overnight.

Results and discussion

Mechanism of the constructed PEC/colorimetric lab-on-paper device

The working principle of the proposed lab-on-paper device based on *in situ* growth of the WO$_3$/BiVO$_4$ heterojunction onto cellulose fibers as a signal amplification probe for PEC/colorimetric sensing of AFP is illustrated in Scheme 1B. To achieve the advantageous PEC sensing mode, BiVO$_4$ with good biocompatibility, which has a narrow band gap, was introduced to WO$_3$ and formed the WO$_3$/BiVO$_4$ heterojunction, which is modified onto the 3D cellulose fibers of the working zone of the PEC detection tab in the lab-on-paper device, exhibiting the admirable PEC performance owing to the unique spatial structure of the functionalized working zone and their preferable morphologies, which could evidently harvest light energy by extending the absorption range, and ultimately improve the intensity of the produced photocurrent. Under irradiation of light, the photoinduced charge carriers of the semiconductor material could remain separated because of their intrinsic electrostatic field. In detail, the photo-induced electrons were transferred from the conduction band of the BiVO$_4$ nanomaterial into WO$_3$ nanosheets, while the holes generated in the valence band of WO$_3$ were transferred into the BiVO$_4$ nanomaterial, which could be consumed by H$_2$O$_2$ electron donors, further enlarging the initial PEC response by the improvement of the separation efficiency of electron-hole carriers. When the AFP targets were introduced by the specifically recognizing interaction with anti-AFP, which is immobilized onto the WO$_3$/BiVO$_4$ heterojunction, a significantly decreased photocurrent signal was produced with obvious steric effects, which are responsive to the concentration change of the target, finally achieving the quantitative PEC detection of AFP. Meanwhile, to realize the colorimetric mode detection of AFP, a colorimetric reaction was introduced by simply altering the device spatial configuration in the presence of WO$_3$/BiVO$_4$ nanoflowers, which could catalyze the TMB oxidation with existing H$_2$O$_2$. In this case, the TMB could lose electrons and transfer into its oxidation products, triggering the colorless solution to turn blue gradually. Accordingly, the proposed lab-on-paper device fabricated by integrating PEC and colorimetric strategies was effectively used for dual-mode ultrasensitive determination of AFP.

Construction and characterization of the dual-mode lab-on-paper device

A three-dimensional (3D) lab-on-paper device was fabricated to achieve PEC/colorimetric dual-mode AFP detection, and its assembly and operation illustration are exhibited in Fig. 1. (i) The designed lab-on-paper device possesses four parts including PEC detection tab, electrode tab (the yellow tab), washing tab, and colorimetric tab. In addition, the whole arrangement is shown in Fig. 1A. (ii) To obtain the PEC signal, the working zone of the PEC detection tab was modified with a layer of Au NPs (the modification process is explained in detail in ESI†) and the WO$_3$/BiVO$_4$ heterojunction was *in situ* grown onto cellulose fibers, as shown in Fig. 1B. (iii) As shown in
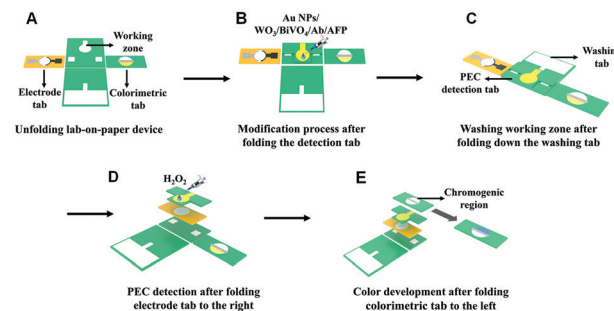

Fig. 1 (A–E) Assembly and operation illustration of the lab-on-paper device. (A) Unfolding the lab-on-paper device. (B) Modification process after folding the detection tab. (C) Washing working zone after folding down the washing tab. (D) PEC detection after folding the electrode tab to the right. (E) Color development after folding the colorimetric tab to the left.

Fig. 1C, the washing tab was folded downward, so that the channel of washing tab could touch the working zone of the detection tab. Therefore, the waste liquid could be collected by the waste pool to treat the liquid waste after each operation. Besides, after PEC detection, the rest liquid was also handled by this folding mode. (iv) In order to realize the dual-mode detection, different folding methods are illustrated in Fig. 1D and E. As illustrated in Fig. 1D, the electrode tab (with a counter and a reference electrode) was projected to right to cover the PEC detection tab. Then, the working zone (a circle of 10 mm in diameter) of the PEC detection tab was folded up to cover the electrode tab to form a three-electrode system. After adding 1.0 mL PBS (pH 6.5, 0.1 M) including 200 μL of H$_2$O$_2$ (5 mM) to the working zone of the detection tab (Fig. 1D), the amplification PEC signal was recorded using a CHI 660D electrochemical workstation. Finally, to achieve the colorimetric detection, the colorimetric tab was folded left, so that the embedded TMB could react with the injected H$_2$O$_2$ (5 mM, 250 μL) in the presence of WO$_3$/BiVO$_4$ nanoflower photoactive materials onto the working zone of the detection tab (Fig. 1E).

To make sure that the WO$_3$/BiVO$_4$ heterojunction was successfully grown onto the surface of cellulose fibers of the lab-on-paper device, the following technologies were applied, such as scanning electron microscopy (SEM), high-resolution transmission electron microscopy (HRTEM), energy-dispersive spectrum (EDS) elemental mapping, X-ray photoelectron spectroscopy (XPS) and X-ray diffraction (XRD). The SEM images in Fig. 2A and its inset image show different magnifications of a bare paper working electrode (PWE), and it can be seen that the bare paper consists of tangled cellulose fibers with porous networks, which could provide the potential platform with a large surface area for the modification of photoactive materials. To improve the conductivity and electron transfer ability of cellulose fibers, a layer of Au NPs was introduced to the surface of cellulose fiber. As shown in Fig. 2B, the uniform and continuous Au NP layer appeared onto the paper fiber surface. Fig. 2C and its inset present the SEM images of different magnifications of the WO$_3$-functionalized Au-PWE (WO$_3$/Au-PWE), which illustrate that

4034 | *J. Mater. Chem. B*, 2022, **10**, 4031–4039

This journal is © The Royal Society of Chemistry 2022
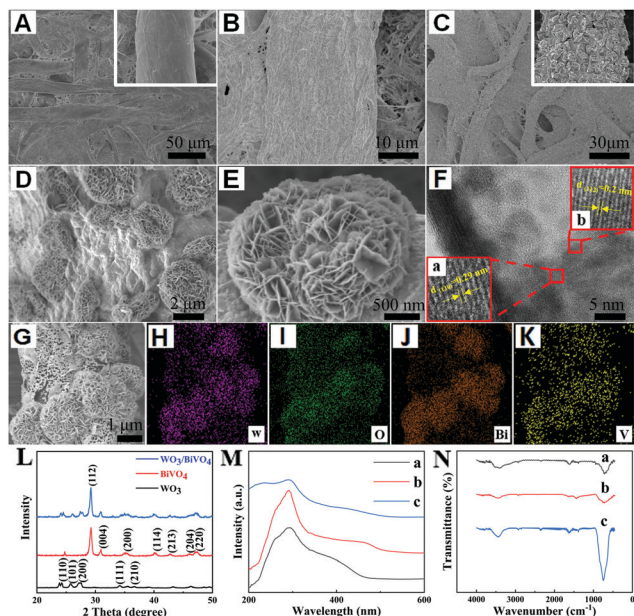
Fig. 2 (A) SEM images of bare a PWE; inset: high-magnification image of bare PWE. (B) SEM image of Au-PWE. (C) WO$_3$/Au-PWE; inset: high-magnification image of WO$_3$/Au-PWE. (D and E) WO$_3$/BiVO$_4$ under different magnifications. (F) HRTEM image of the WO$_3$/BiVO$_4$ heterojunction (inset (a): the lattice of WO$_3$; inset (b): the lattice of BiVO$_4$). (G–K) Elemental mapping SEM mode of W, O, Bi, and V and the corresponding SEM image. (L) XRD patterns of WO$_3$, BiVO$_4$, and WO$_3$/BiVO$_4$. (M) UV-vis absorption spectrum of WO$_3$ (curve a), BiVO$_4$ (curve b), and WO$_3$/BiVO$_4$ (curve c). (N) FT-IR spectra of (a) WO$_3$, (b) BiVO$_4$, and (c) WO$_3$/BiVO$_4$.

the WO$_3$ nanoplate was densely grown on the cellulose fiber surface, making it a larger specific surface area to load more BiVO$_4$. The SEM images of WO$_3$/BiVO$_4$ heterojunctions are displayed in Fig. 2D and E, which clearly show nanoflower morphologies with a diameter of about 2.3 μm. The special nanoflower structure with a large specific surface area is beneficial for constructing the sensing platform. Fig. 2F shows the HRTEM image of the WO$_3$/BiVO$_4$ heterojunction and its inset a matched with the WO$_3$(110) plane, 0.29 nm in size, and inset b agreed well with BiVO$_4$(112), 0.2 nm in size. In addition, the elemental mapping under the SEM mode was applied to illustrate the presence of W, O, Bi, and V elements in a single WO$_3$/BiVO$_4$ nanoflower. The corresponding mapping SEM images are shown in Fig. 2G–K, which clearly show that the WO$_3$/BiVO$_4$ nanoflower was successfully synthesized. Besides, the energy-dispersive spectrum (EDS) mappings of different elements displayed in Fig. S5 (ESI†) clearly show the presence of W, O, Bi, and V elements, which demonstrated the successful synthesis of WO$_3$/BiVO$_4$ nanoflowers.

XRD was performed to identify the crystal structure of the proposed WO$_3$/BiVO$_4$ heterojunction. It is seen from the XRD image, as exhibited in Fig. 2L, that there are a series of diffraction peaks at 24.3, 26.8, 28.2, 33.5, and 37.6°, which are assigned to the (110), (101), (200), (111), and (210) crystal planes of WO$_3$, and the other diffraction peaks appear at 28.6, 30.9, 34.5, 39.7, 45.5, 47.0, and 49.6° which correspond to the (112), (004), (200), (114), (213), (204), and (220) crystal planes of

BiVO$_4$. The blue curve of the XRD patterns of WO$_3$/BiVO$_4$ nanoflowers was consistent with pure WO$_3$ and BiVO$_4$ XRD patterns, which clearly show that the WO$_3$/BiVO$_4$ heterojunction was successfully synthesized. To further verify the synthesized WO$_3$/BiVO$_4$ heterostructure, the ultraviolet-visible (UV-vis) absorption spectra and Fourier transform infrared (FT-IR) spectra were also adopted. As shown in Fig. 2M, the UV-vis absorption spectrum of WO$_3$/BiVO$_4$ (curve c) shows a wider absorption range than that of WO$_3$ (curve a), indicating that the WO$_3$/BiVO$_4$ heterojunction enhanced the light harvesting ability. Consequently, the extended light absorption capacity of WO$_3$/BiVO$_4$ was conducive to amplify the photo-to-current conversion efficiency. The results from the Tauc plots (Fig. S6A, ESI†) also demonstrated the effect of heterojunction formation on the photoactive materials. Fig. 2N shows the IR spectra over the range of 500–4000 cm^{-1} at room temperature. The results indicate the different modes of vibrations of molecules with their associated energies in the infrared region. The representative absorption peak at 948 cm^{-1} observed in the WO$_3$ (curve a) was the fundamental vibration, which was assigned to W–O. What is more, curve b represents BiVO$_4$, and the peaks at 730 and 834 cm^{-1} in curve b belong to the asymmetric stretching and symmetric vibration of VO$_4^{3-}$ tetrahedron. Accordingly, the WO$_3$/BiVO$_4$ heterojunction synthesis was successfully realized (curve c).[44,64] In addition, an elemental analysis of XPS technique was also carried out to confirm the successful preparation of the WO$_3$/BiVO$_4$ heterojunction. As exhibited in Fig. 3, the chemical states of W, O, Bi, and V elements in WO$_3$/BiVO$_4$ were investigated by XPS analysis. It can be seen that all the peak positions of WO$_3$/BiVO$_4$ in the XPS spectra were demarcated with C 1s at 281.9 eV. As shown in Fig. S8 (ESI†), the full survey spectrum results prove the existence of W, O, Bi, and V elements. The main XPS elemental spectra of W, O, Bi, and V elements are demonstrated in Fig. 3A–D. Fig. 3A shows two strength peaks at 32.4 and
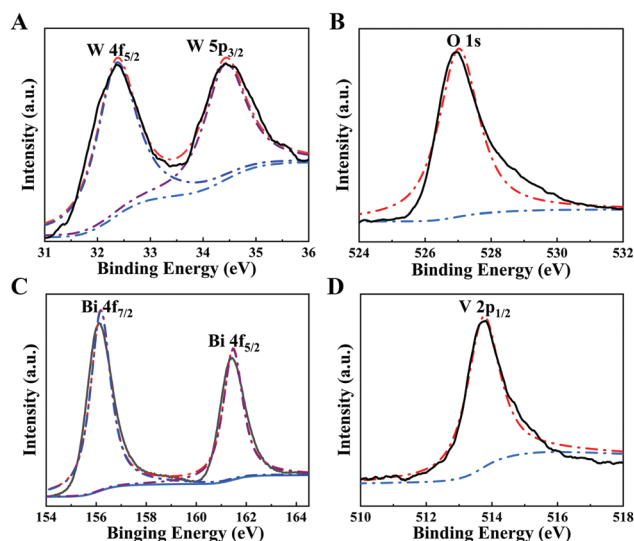

Fig. 3 XPS spectrum of the WO$_3$/BiVO$_4$ heterojunction: (A) W 4f. (B) O 1s. (C) Bi 4f. (D) V 2p.

This journal is © The Royal Society of Chemistry 2022

J. Mater. Chem. B, 2022, 10, 4031–4039 | 4035

34.4 eV, which are ascribed to the high oxidation state of W in WO_3.[65] The peak in Fig. 3B at 527.02 eV belongs to the lattice oxygen. Fig. 3C demonstrates two peaks of 156.18 and 161.47 eV, which could be attributed to Bi $4f_{7/2}$ and Bi $4f_{5/2}$ in the spin–orbit splitting of Bi^{3+}. The peak of V 2p in Fig. 3D belongs to V^{5+} in $BiVO_4$.[66] All of the above-mentioned results illustrated the successful preparation of the $WO_3/BiVO_4$ heterojunction.

PEC and electrochemical characterization of the fabricated lab-on-paper device

To investigate the photoresponse performance of the as-prepared device, the transient photocurrent investigation was conducted by chronoamperometry under chopped light illumination. As exhibited in Fig. 4A, the photoresponse of the proposed device with various modification processes was measured at an applied bias potential of 0.4 V under light irradiation with on-off cycles. Compared with the bare $BiVO_4$ electrode (curve a), a stronger photocurrent of $WO_3/BiVO_4$ (curve b) was achieved under illumination, evidentially suggesting the improvement of separation efficiency of electron–hole carriers by introduction of $BiVO_4$ into WO_3 to form $WO_3/BiVO_4$ heterojunctions. After modifying with CS, Ab, BSA and AFP onto a $WO_3/BiVO_4$ heterojunction-functionalized cellulose paper electrode, a descending trend of photocurrent intensity of the obtained photoelectrode appears with $WO_3/BiVO_4/CS$ (curve c) > $WO_3/BiVO_4/CS/Ab$ (curve d) > $WO_3/BiVO_4/CS/Ab/BSA$ (curve e) > $WO_3/BiVO_4/CS/Ab/BSA/AFP$ (curve f) because the relative insulative proteins could inhibit sacrificial agent diffusion to the electrode surface and further decrease the photocurrent intensity.[8] Meanwhile, the successively decreased photocurrent intensity indicated the successful immobilization of these proteins onto the photoelectrode. For further investigating the assembly process of the proposed photoelectrode and its interface electron transfer activity, electrochemical impedance spectroscopy (EIS) was performed. Fig. 4B illustrates the electrochemical impedance Nyquist plot of the various modified process of the proposed photoelectrode with $[Fe(CN)_6]^{3-/4-}$ for the redox probe. In addition, the Nyquist

plot included a semicircle sector and a linear sector, where the diameter of the semicircle could directly express the interface electron transfer resistance (R_{et}) of the photoelectrode.[46] It can be seen that R_{et} of $WO_3/BiVO_4$ (curve b) was smaller than WO_3 (curve a) due to the quick electron transfer of the $WO_3/BiVO_4$ sensing interface, whereas when CS was introduced into the surface of the electrode, the R_{et} value of $WO_3/BiVO_4/CS$ increased significantly (curve c) owing to the obstructing effect of the modified biomolecules for the ferricyanide diffusion to the surface of electrode. In addition, upon incubation of anti-AFP on the electrode surface, the R_{et} value increased more (curve d) because of the poor electron transfer ability. Finally, after BSA was added to the surface of the electrode to block the active sites, the value of R_{et} continued to increase (curve e), resulting from the poor conductivity of organic molecules as well as impeding the $[Fe(CN)_6]^{3-/4-}$ transfer to the photoelectrode surface. Accordingly, the obtained EIS results of each modification step indicated the successful construction of the lab-on-paper device.

Analytical performance of the lab-on-paper device for PEC/colorimetric of AFP immunosensing

To obtain the optimum PEC signal of the prepared sensing platform, experimental conditions including applied potential, the pH of electrolyte, the synthesis time of photoactive materials, and the incubation time of AFP were carefully investigated. (The details and the obtained results are illustrated in ESI† and Fig. S9, respectively.) Under the optimal experimental conditions, the analytical performance of the as-prepared PEC immunosensor was investigated by recording the photocurrents to different concentrations of AFP. As the AFP concentration increased from 0.1 to 100 ng mL^{-1}, the photocurrent decreased accordingly because the more incubated AFP could inhibit more H_2O_2 in contact with the photoelectrode surface (Fig. 5A). As shown in Fig. 5B, the calibration plots indicated that the PEC signal decrement was proportional to the AFP concentrations logarithmically in the 0.09–100 ng mL^{-1} range. The linear equation is as follows: $I = -3.32 \log c_{AFP} + 9.70$ ($R^2 = 0.997$), and the limit of detection (LOD) is 0.03 ng mL^{-1} with a signal-to-noise (S/N) ratio of 3. Compared with previous reported works (Table 1: comparison of several immunosensors of AFP detection and Table S1 (ESI†): comparison with other PEC-based AFP biosensors), the proposed PEC immunosensor presented a wide linear range and low LOD, which could be attributed to the good property of the synthesized photoelectrode material and low background noise of PEC technical assay. What is more, the corresponding colorimetric detection could be realized by folding the colorimetric tab of the fabricated device. After introduction of H_2O_2 into the colorimetric tab, the enhanced catalytic activity of $WO_3/BiVO_4$ could catalyze TMB, which was simply pre-embedded at the detection zone of the colorimetric tab of the prepared lab-on-paper device to produce ox-TMB with a blue product. In this way, AFP could be detected by the color intensity of the colorimetric tab, realizing the colorimetric signal readout for AFP target semi-quantitative detection. The real images of colorimetric
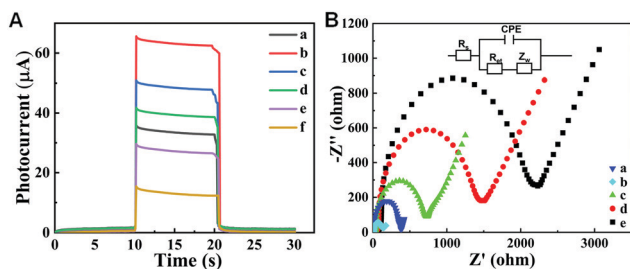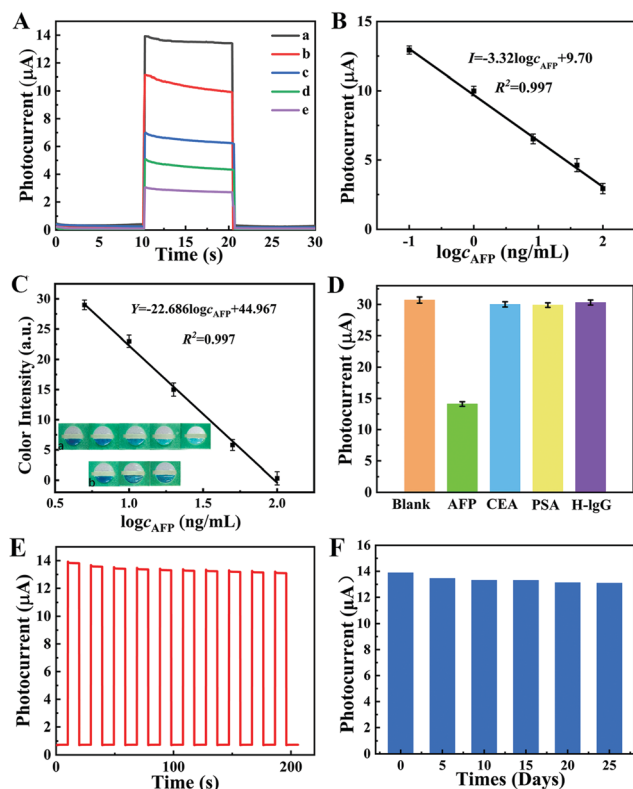

Fig. 4 (A) Photocurrent responses of the modified electrode in PBS (0.1 M, pH 6.6) containing 5 mM H_2O_2 at 0.4 V: (a) $BiVO_4$, (b) $WO_3/BiVO_4$, (c) $WO_3/BiVO_4/CS$, (d) $WO_3/BiVO_4/CS/Ab$, (e) $WO_3/BiVO_4/CS/Ab/BSA$, and (f) $WO_3/BiVO_4/CS/Ab/BSA/AFP$ (c_{AFP} = 0.1 ng mL^{-1}). (B) Electrochemical impedance spectroscopy (EIS) for each modification process in PBS (0.1 M, pH 7.4) containing 5.0 mM $[Fe(CN)_6]^{3-/4-}$ and 0.1 M KCl: (a) WO_3, (b) $WO_3/BiVO_4$, (c) $WO_3/BiVO_4/CS$, (d) $WO_3/BiVO_4/CS/Ab$, and (e) $WO_3/BiVO_4/CS/Ab/BSA$.

4036 | *J. Mater. Chem. B*, 2022, **10**, 4031–4039

This journal is © The Royal Society of Chemistry 2022

Fig. 5 (A) Photocurrent responses of different concentrations of AFP at 0.1, 1, 10, 50, and 100 ng mL^{-1} (a–e). (B) Corresponding calibration curve. (C) Calibration curve of color intensity *versus* the logarithm of AFP (inset a: images of the corresponding chromogenic reactions; inset b: colorimetric sensing results of clinical serum with c_{AFP} = 10 ng mL^{-1}). (D) Selectivity of the proposed PEC assay of AFP (c_{AFP} = 0.1 ng mL^{-1}). (E) Stability of the photocurrent within 200 s (c_{AFP} = 0.1 ng mL^{-1}). (F) Stability of the proposed biosensor for different periods of storage: 0 days, 5 days, 10 days, 15 days, 20 days, and 25 days (c_{AFP} = 0.1 ng mL^{-1}). The error bar represents the standard deviation of five repeated tests. All photocurrent measurements were carried out in 0.1 M PBS (pH 6.6) containing 5 mM H$_2$O$_2$. The applied potential was 0.4 V.

Table 1 Comparison of several immunosensors of AFP detection

Method	Detection range (ng mL^{-1})	LOD	Ref.
ELISA	0.1–100	1 ng mL^{-1}	67
ECL	0.5–20	0.1 ng mL^{-1}	68
Electrochemical	10^2–10^5	50 ng mL^{-1}	69
Chemiluminescence	10–150	7.2 pg mL^{-1}	70
PEC	0.09–100	0.03 ng mL^{-1}	This work

detection and the calibration curve can be seen in Fig. 5C. The corresponding linear equation is $Y = -22.686 \log c_{AFP} + 44.967$ (R^2 = 0.997) and the colorimetric LOD is 1.47 ng mL^{-1} with a linear range of 5–100 ng mL^{-1}. Besides, the color changes from dark blue to cyan in colorimetric sensing with the increase in AFP concentration (as shown in inset a). Besides, in order to investigate the selectivity of the as-prepared sensing platform, the photocurrent signal of the lab-on-paper device was recorded when the device was incubated with different targets, AFP, CEA,

PSA, and H-IgG, under the same experimental conditions (colorimetric experiments of selectivity experiments are shown in Fig. S10, ESI†). As shown in Fig. 5D, the photocurrent intensities of CEA, PSA, and H-IgG are similar to that of the blank experiment, and far more than that of the AFP sample, indicating the good selectivity of the as-prepared lab-on-paper device for detecting AFP with the signal-off PEC strategy. Fig. 5E shows the stability of the photocurrent responses of the PEC sensing platform. The photocurrent signals were recorded as the excitation light was turned on and off for 10 s about 10 times. Record 200 s later, the photocurrent response in Fig. 5E illustrates that the photocurrent can still reach about 95% compared with its initial photocurrent value, illustrating the good long-term stability of the prepared lab-on-paper device. In addition, the relative standard deviation (RSD) was less than 2%, certifying the good stability of the fabricated biosensor. Besides, to investigate the effects of different days of storage on the proposed biosensor, the photocurrent of the proposed biosensor stored at 4 °C was measured every 5 days after incubation with 0.1 ng mL^{-1} AFP (Fig. 5F). After 25 days, the current response generated by the proposed biosensor could still reach 94% of the initial signal, which indicated that the proposed paper chip has credible stability.

Application in human serum sample

To verify the practical application of the as-prepared dual-mode lab-on-paper device, clinical serum samples were detected. Briefly, real human serum samples were collected from the whole blood by centrifugation (10 000 rpm, 8 min). The supernatant was diluted and different concentrations of AFP were added. The analytical performance of serum sample-mixed AFP was investigated, and the findings (the average of three parallel experimental results) are shown in Table 2. It can be seen that the RSD and the recovery rate were from 1.17% to 5.6% and from 94.7% to 101.4%, respectively. The above-mentioned results indicated that the build device could accomplish clinical applications of AFP in human serum samples (ESI† shows more details). At the same time, colorimetric experiments in clinical serum were also investigated (colorimetric sensing results of clinical serum are illustrated in Fig. 5C), illustrating that the as-prepared lab-on-paper device could be utilized as a potential candidate for the clinical AFP detection.

Table 2 Determination of different concentrations of AFP incorporated into human serum by the proposed lab-on-paper device

Serum sample	Added,[a] M	Found, M	Recovery,[b] %	RSD, %
1	1×10^{-9}	9.47×10^{-10}	94.7	5.6
2	5×10^{-9}	5.07×10^{-9}	101.4	1.38
3	1×10^{-8}	9.87×10^{-9}	98.7	1.17
4	5×10^{-8}	4.85×10^{-8}	97.0	3.09
5	1×10^{-7}	9.76×10^{-8}	97.6	2.46

[a] The different concentration of AFP standards were added into the initial human serum samples, respectively. [b] The recovery was calculated by the value (the found concentration subtracted that of PEC immunoassay) relative to the added AFP level.

This journal is © The Royal Society of Chemistry 2022

J. Mater. Chem. B, 2022, 10, 4031–4039 | 4037

Conclusions

In summary, a dual-mode PEC/colorimetric lab-on-paper device has been successfully fabricated based on *in situ* growth of WO_3/$BiVO_4$ heterojunctions onto cellulose fibers for the ultrasensitive detection of AFP. The as-prepared WO_3/$BiVO_4$ nanoflower was well characterized by various techniques including SEM, EDS, HRTEM, XRD, UV-vis, FT-IR spectroscopy, and XPS. On account of the admirable PEC response and enhanced catalytic activity of WO_3/$BiVO_4$ nanoflower *in situ* growth onto the 3D cellulose fibers of the designed lab-on-paper device, the highly reliable PEC signal and colorimetric signal readout system for ultrasensitive AFP detection and semi-quantitative AFP detection has been successfully obtained. Besides, by the smart layout of the lab-on-paper device for conversion treatment between hydrophobicity and hydrophilicity, the washing issue in the operational process of the lab-on-paper device was easily solved by manually folding the washing tab of the device. We believe that the provided approach could provide an extensive strategy with features of simple and convenient operation processes for the ultrasensitive dual-mode determination of different kinds of biomarkers based on the lab-on-paper device.

Author contributions

Xu Li: investigation, methodology, writing-original draft. Kang Cui: conceptualization, supervision, writing-reviewing and editing. Mingzhen Xiu: investigation, methodology, data curation. Chenxi Zhou: investigation, formal analysis. Li Li: investigation, formal analysis. Jing Zhang: formal analysis, visualization. Shiji Hao: investigation, formal analysis. Lina Zhang: editing, resources. Shenguang Ge: conceptualization, investigation. Yizhong Huang: investigation, resources, funding acquisition. Jinghua Yu: funding acquisition, project administration.

Conflicts of interest

The authors declare no competing financial interests.

Acknowledgements

References

1 T. B. Tomasi, Jr., *Annu. Rev. Med.*, 1977, **28**, 453–465.
2 T. Yamashita, M. Forgues, W. Wang, J. W. Kim, Q. Ye, H. Jia, A. Budhu, K. A. Zanetti, Y. Chen, L. X. Qin, Z. Y. Tang and X. W. Wang, *Cancer Res.*, 2008, **68**, 1451–1461.
3 X. Huo, P. Liu, J. Zhu, X. Liu and H. Ju, *Biosens. Bioelectron.*, 2016, **85**, 698–706.
4 J. Lin, C. He, L. Zhang and S. Zhang, *Anal. Biochem.*, 2009, **384**, 130–135.
5 Z. Song, R. Yuan, Y. Chai, Y. Zhuo, W. Jiang, H. Su, X. Che and J. Li, *Chem. Commun.*, 2010, **46**, 6750–6752.
6 H. Ikeda, Y. Sato, N. Yoneda, K. Harada, M. Sasaki, S. Kitamura, Y. Sudo, A. Ooi and Y. Nakanuma, *Hum. Pathol.*, 2012, **43**, 1955–1963.
7 X. Li, X. Pan, J. Lu, Y. Zhou and J. Gong, *Biosens. Bioelectron.*, 2020, **158**, 112158.
8 J. Chen and G. C. Zhao, *Biosens. Bioelectron.*, 2017, **98**, 155–160.
9 D. Pan, K. Chen, Q. Zhou, J. Zhao, H. Xue, Y. Zhang and Y. Shen, *Biosens. Bioelectron.*, 2019, **131**, 178–184.
10 Q. Zhou, H. Xue, Y. Zhang, Y. Lv, H. Li, S. Liu, Y. Shen and Y. Zhang, *ACS Sens.*, 2018, **3**, 1385–1391.
11 K. H. Kim, S. Y. Lee, D. G. Kim, S. Y. Lee, J. Y. Kim and J. S. Yoo, *Anal. Chem.*, 2020, **92**, 12588–12595.
12 R. T. Ma, X. B. Zhao, X. Y. Sun, J. Liu, W. Ha and Y. P. Shi, *J. Mater. Chem. B*, 2019, **7**, 6187–6194.
13 S. Zhao, N. Liu, W. Wang, Z. Xu, Y. Wu and X. Luo, *Biosens. Bioelectron.*, 2021, **190**, 113466.
14 T. Feng, X. Qiao, H. Wang, Z. Sun, Y. Qi and C. Hong, *J. Mater. Chem. B*, 2016, **4**, 990–996.
15 X. Zhu, Q. Zhai, W. Gu, J. Li and E. Wang, *Anal. Chem.*, 2017, **89**, 12108–12114.
16 J. Zhang, S. Wang, K. Liu, Y. Wei, X. Wang and Y. Duan, *Anal. Chem.*, 2015, **87**, 2959–2965.
17 X. Bi and Z. Liu, *Anal. Chem.*, 2014, **86**, 959–966.
18 X. Li, Z. Zheng, X. Liu, S. Zhao and S. Liu, *Biosens. Bioelectron.*, 2015, **64**, 1–5.
19 Q. Zhou, G. Li, K. Chen, H. Yang, M. Yang, Y. Zhang, Y. Wan, Y. Shen and Y. Zhang, *Anal. Chem.*, 2020, **92**, 983–990.
20 W. Yang, X. Wang, W. Hao, Q. Wu, J. Peng, J. Tu and Y. Cao, *J. Mater. Chem. B*, 2020, **8**, 2363–2370.
21 P. P. Li, Y. Cao, C. J. Mao, B. K. Jin and J. J. Zhu, *Anal. Chem.*, 2019, **91**, 1563–1570.
22 N. Hao, J. Lu, M. Chi, M. Xiong, Y. Zhang, R. Hua and K. Wang, *J. Mater. Chem. B*, 2019, **7**, 1133–1141.
23 J. Shu and D. Tang, *Anal. Chem.*, 2020, **92**, 363–377.
24 J. Shu and D. Tang, *Chem. – Asian J.*, 2017, **12**, 2780–2789.
25 Y. Gao, Y. Zeng, X. Liu and D. Tang, *Anal. Chem.*, 2022, **94**, 4859–4865.
26 A. Victorious, S. Saha, R. Pandey and L. Soleymani, *Angew. Chem., Int. Ed.*, 2021, **60**, 7316–7322.
27 X. Xiang, Y. Wang, Y. Zhang, R. Yuan and S. Wei, *Chem. Commun.*, 2021, **57**, 12480–12483.
28 Z. Li, H. Yang, M. Hu, L. Zhang, S. Ge, K. Cui and J. Yu, *ACS Appl. Mater. Interfaces*, 2020, **12**, 17177–17184.
29 F. Li, S. Wang, H. Yin, Y. Chen, Y. Zhou, J. Huang and S. Ai, *ACS Sens.*, 2020, **5**, 1092–1101.

4038 | *J. Mater. Chem. B*, 2022, **10**, 4031–4039

This journal is © The Royal Society of Chemistry 2022

30 M. Hao, P. Miao, Y. Wang, W. Wang, S. Ge, X. Yu, X. X. Hu, B. Ding, J. Zhang and M. Yan, *Anal. Chem.*, 2021, **93**, 11251–11258.

31 J. Xue, C. Gao, L. Zhang, K. Cui, W. He and J. Yu, *J. Mater. Chem. B*, 2018, **6**, 4697–4703.

32 B. R. Lee, M. G. Lee, H. Park, T. H. Lee, S. A. Lee, S. S. M. Bhat, C. Kim, S. Lee and H. W. Jang, *ACS Appl. Mater. Interfaces*, 2019, **11**, 20004–20012.

33 J. Wang, Y. Pan, L. Jiang, M. Liu, F. Liu, M. Jia, J. Li and Y. Lai, *ACS Appl. Mater. Interfaces*, 2019, **11**, 37541–37549.

34 S. Zhang, L. Feng, P. Li, L. Zhang, X. Chen, S. Chu, Y. Gao, S. Xie, J. Jiang and H. Wang, *J. Mater. Chem. B*, 2021, **9**, 5869–5876.

35 G. Sun, P. Wang, P. Zhu, L. Ge, S. Ge, M. Yan, X. Song and J. Yu, *J. Mater. Chem. B*, 2014, **2**, 4811–4817.

36 X. Zhang, H. Wang, J. Zhang, J. Li, Z. Ma, J. Li, B. Leng, P. Niu and B. Liu, *Nano Energy*, 2020, **77**, 105119.

37 S. Lv, K. Zhang, L. Zhu and D. Tang, *Anal. Chem.*, 2020, **92**, 1470–1476.

38 D. Fan, C. Bao, X. Liu, D. Wu, Y. Zhang, H. Wang, B. Du and Q. Wei, *J. Mater. Chem. B*, 2018, **6**, 7634–7642.

39 S. H. Baeck, K. S. Choi, T. F. Jaramillo, G. D. Stucky and E. W. McFarland, *Adv. Mater.*, 2003, **15**, 1269–1273.

40 S. S. Kalanur, Y. J. Hwang, S. Y. Chae and O. S. Joo, *J. Mater. Chem. A*, 2013, **1**, 3479–3488.

41 Y. Wang, W. Tian, L. Chen, F. Cao, J. Guo and L. Li, *ACS Appl. Mater. Interfaces*, 2017, **9**, 40235–40243.

42 Y. Pihosh, I. Turkevych, K. Mawatari, T. Asai, T. Hisatomi, J. Uemura, M. Tosa, K. Shimamura, J. Kubota, K. Domen and T. Kitamori, *Small*, 2014, **10**, 3692–3699.

43 P. Zhang and X. W. D. Lou, *Adv. Mater.*, 2019, **31**, e1900281.

44 J. H. Kim and J. S. Lee, *Adv. Mater.*, 2019, **31**, e1806938.

45 H. Zhang, W. Zhou, Y. Yang and C. Cheng, *Small*, 2017, **13**, 1603840.

46 S. Z. Lv, K. Y. Zhang, Y. Y. Zeng and D. P. Tang, *Anal. Chem.*, 2018, **90**, 7086–7093.

47 J. Shu, Z. Qiu, Z. Lin, G. Cai, H. Yang and D. Tang, *Anal. Chem.*, 2016, **88**, 12539–12546.

48 S. Xu, B. Dai, W. Zhao, L. Jiang and H. Huang, *Anal. Chem. Acta*, 2020, **1120**, 1–10.

49 S. Ge, L. Zhang, Y. Zhang, F. Lan, M. Yan and J. Yu, *Nanoscale*, 2017, **9**, 4366–4382.

50 C. Li, Y. Liu, X. Zhou and Y. Wang, *J. Mater. Chem. B*, 2020, **8**, 3582–3589.

51 K. Cui, C. Zhou, B. Zhang, L. Zhang, Y. Liu, S. Hao, X. Tang, Y. Huang and J. Yu, *ACS Appl. Mater. Interfaces*, 2021, **13**, 33937–33947.

52 Y. Zhang, J. Xu, S. Zhou, L. Zhu, X. Lv, J. Zhang, L. Zhang, P. Zhu and J. Yu, *Anal. Chem.*, 2020, **92**, 3874–3881.

53 H. Wang, C. Zhou, X. Sun, Y. Jian, Q. Kong, K. Cui, S. Ge and J. Yu, *Biosens. Bioelectron.*, 2018, **117**, 651–658.

54 R. Liu, E. M. McConnell, J. Li and Y. Li, *J. Mater. Chem. B*, 2020, **8**, 3213–3230.

55 Y. Soda, D. Citterio and E. Bakker, *ACS Sens.*, 2019, **4**, 670–677.

56 J. Sun, L. Li, S. Ge, P. Zhao, P. Zhu, M. Wang and J. Yu, *ACS Appl. Mater. Interfaces*, 2021, **13**, 3645–3652.

57 R. Ota, K. Yamada, K. Suzuki and D. Citterio, *Analyst*, 2018, **143**, 643–653.

58 X. Yin, L. Liang, P. Zhao, F. Lan, L. Zhang, S. Ge and J. Yu, *J. Mater. Chem. B*, 2018, **6**, 5795–5801.

59 F. Liu, S. Ge, J. Yu, M. Yan and X. Song, *Chem. Commun.*, 2014, **50**, 10315–10318.

60 C. Zhou, K. Cui, Y. Liu, S. Hao, L. Zhang, S. Ge and J. Yu, *Anal. Chem.*, 2021, **93**, 5459–5467.

61 F. Mustafa and S. Andreescu, *ACS Sens.*, 2020, **5**, 4092–4100.

62 Y. Liu, K. Cui, Q. Kong, L. Zhang, S. Ge and J. Yu, *Biosens. Bioelectron.*, 2020, **148**, 111839.

63 Q. Han, L. Li, W. Gao, Y. Shen, L. Wang, Y. Zhang, X. Wang, Q. Shen, Y. Xiong, Y. Zhou and Z. Zou, *ACS Appl. Mater. Interfaces*, 2021, **13**, 15092–15100.

64 W. Lai, Z. Chen, S. Ye, Y. Xu, G. Xie, C. Kuang, Y. Li, L. Zheng and L. Wei, *J. Hazard. Mater.*, 2021, **408**, 124621.

65 Q. Pan, H. Zhang, Y. Yang and C. Cheng, *Small*, 2019, **15**, e1900924.

66 Y. Qiu, W. Liu, W. Chen, W. Chen, G. Zhou, P. C. Hsu, R. Zhang, Z. Liang, S. Fan, Y. Zhang and Y. Cui, *Sci. Adv.*, 2016, **2**, e1501764.

67 P. Preechakasedkit, W. Siangproh, N. Khongchareonporn, N. Ngamrojanavanich and O. Chailapakul, *Biosens. Bioelectron.*, 2018, **102**, 27–32.

68 X. L. Liang, N. Bao, X. Luo and S. N. Ding, *Biosens. Bioelectron.*, 2018, **117**, 145–152.

69 G. Li, S. Li, Z. Wang, Y. Xue, C. Dong, J. Zeng, Y. Huang, J. Liang and Z. Zhou, *Anal. Biochem.*, 2018, **547**, 37–44.

70 J. Liu, J. Zhao, S. Li, L. Zhang, Y. Huang and S. Zhao, *Talanta*, 2017, **165**, 107–111.

This journal is © The Royal Society of Chemistry 2022

J. Mater. Chem. B, 2022, **10**, 4031–4039 | **4039**